Scattering information obtained by optical microscopy: Differential dynamic microscopy and beyond

Fabio Giavazzi,[1,*] Doriano Brogioli,[2] Veronique Trappe,[3] Tommaso Bellini,[1] and Roberto Cerbino[1,†]
[1]*Dipartimento di Chimica, Biochimica a Biotecnologie per la Medicina, Università degli Studi di Milano, via Fratelli Cervi 93, Segrate, Milano I-20090, Italy*
[2]*Dipartimento di Medicina Sperimentale, Università degli Studi di Milano–Bicocca, via Cadore 48, Monza, Milano I-20052, Italy*
[3]*Department of Physics, University of Fribourg, Chemin du Musée 3, CH-1700 Fribourg, Switzerland*

We describe the use of a bright-field microscope for dynamic light scattering experiments on weakly scattering samples. The method is based on collecting a time sequence of microscope images and analyzing them in the Fourier space to extract the characteristic time constants as a function of the scattering wave vector. We derive a theoretical model for microscope imaging that accounts for (a) the three-dimensional nature of the sample, (b) the arbitrary coherence properties of the light source, and (c) the effect of the finite numerical aperture of the microscope objective. The model is tested successfully against experiments performed on a colloidal dispersion of small spheres in water, by means of the recently introduced differential dynamic microscopy technique [R. Cerbino and V. Trappe, Phys. Rev. Lett. **100**, 188102 (2008)]. Finally, we extend our model to the class of microscopy techniques that can be described by a linear space-invariant imaging of the density of the scattering centers, which includes, for example, dynamic fluorescence microscopy.

I. INTRODUCTION

Scattering and microscopy are traditionally considered as two complementary techniques for the investigation of soft and biological materials [1]. Scattering provides in a single shot a powerful average information from the entire sample, while microscopy allows for a detailed study of the behavior of a small portion of it. As far as dynamic measurements are concerned, both approaches offer interesting possibilities. In the real space it is possible to characterize the motion of moving entities by tracking their position in time. This approach is known as video particle tracking (VPT) [2,3]. In the reciprocal space one can obtain equivalent information by monitoring the temporal intensity fluctuations associated with the sample dynamics [4]. This approach is known as dynamic light scattering (DLS).

The possibility of combining scattering and microscopy in a single instrument has been already exploited in the past (see, for example, Ref. [5] and references therein). In most cases a commercial microscope was customized and equipped with a laser source, a suitable optics, and a hardware for both the imaging of the sample (VPT) and the calculation of statistical properties of the scattered light (DLS). In particular the Fourier transform (FT) operation, needed to operate in the reciprocal space, was realized by means of an auxiliary lens and the intensity distribution in the back focal plane of the lens was analyzed (Fourier microscopy).

It has been recently proposed that equivalent results can be obtained by collecting and processing images close to the sample [6–9]. Sequences of *real-space* images are Fourier analyzed and wave vector resolved information about the system structure and dynamics can be extracted. With reference to dynamics studies, this approach has been successfully demonstrated with (spatially coherent) monochromatic [10,11] and quasimonochromatic [12–14] light. The close proximity of the detector to the sample is necessary for the success of the above-mentioned approach. When a sample is illuminated with a large coherent beam, it exists a region—the deep Fresnel region—where the transverse correlation properties of the scattered light are independent on the distance from the sample [7,8,15,16]. It is only within the deep Fresnel region that it is possible to recover a scattering pattern of the sample by numerical Fourier analysis of the images. In a general way this defines a whole family of techniques that we refer to as *near-field*, or *deep Fresnel*, scattering [17].

In near-field scattering experiments with coherent illumination the deep Fresnel region can be very extended. In the attempt of maximizing the scattering signal at the lowest wave vectors, it is a common practice to operate at large (from a few millimeters up to 1 m) defocusing distances from the sample. At such distances the defocused images are either shadowgrams [6,10,12–14] or *speckle images* [7–9,11]. Very recently it has been attempted to extend the near-field scattering family to progressively incoherent illumination. Experiments demonstrated that the requirements in terms of both spatial and temporal coherences can be largely relaxed either for partially coherent x rays [18] or for bright-field microscopy [19]. Working with low-coherence sources reduces the extent of the deep Fresnel region and forces collecting images closer to the sample. This has been done in Ref. [19] where the microscope object plane was chosen at the sample midplane. The use of low-coherence sources offers unexpected advantages, especially when the samples are confined in thin cells. A small value of the longitudinal coherence length minimizes the tedious Fabry-Perot interference fringes observed with laser illumination. In addition a close distance to the sample guarantees a good correspon-

*fabio.giavazzi@unimi.it
†roberto.cerbino@unimi.it

dence between the image intensity and the local density of scatterers within the sample. A better quantification of this correspondence is of paramount importance in view of future extensions of near-field scattering techniques to systems whose dynamical properties are not uniform in space (heterogeneous dynamics) [20]. Moreover, the question about the possible limitations due to the loss of coherence remains to be addressed.

In this paper we present a description of the scattering-based image formation process with partially coherent illumination, including the effect of out-of-focus planes in the microscope images. The main focus here is on the application of such a description to the microscope-based investigation of dynamical systems, with a special reference to the results presented in Ref. [19]. Our results suggest that dynamic microscopy techniques, and in particular differential dynamic microscopy (DDM) [19], can be quite flexible diagnostic tools for the study of dynamical phenomena, in particular for those laboratories that are already equipped with a microscope. We generalize our results to all those cases where the imaging is a linear space-invariant process, including fluorescence microscopy. The paper structure is as follows. In Sec. II we present experimental results on colloidal samples obtained with DDM and provide a two-dimensional (2D) model of dynamic microscopy experiments in the Fourier space, along the line followed in Ref. [19]. In Sec. III we give a fully quantitative theory for the three-dimensional (3D) bright-field imaging of weak scattering objects, i.e., that do not dephase or absorb light too strongly. In Sec. IV we treat the more general case of linear space-invariant imaging and provide theoretical results for the case of fluorescence imaging as an example. In Sec. V we describe various approaches to the analysis of time series of microscopy images.

II. ROUTE TO THE DESCRIPTION OF DYNAMIC MICROSCOPY EXPERIMENTS IN THE FOURIER SPACE

To introduce dynamic microscopy in the Fourier space, we first present in this section the data obtained by applying the DDM technique to a series of microscopy images, obtained by using a Brownian colloidal dispersion as a sample. However, we stress that DDM is just one of the methods that can be used to perform dynamic microscopy experiments in the Fourier space. Alternative algorithms will be presented in Sec. V. The DDM data presented here will be used throughout the paper to test the theoretical descriptions of scattering-based image formation, which we introduce stepwise.

As a first step we discuss the DDM data in the frame of a simplified two-dimensional model, introduced in Ref. [19]. Our experimental system is a dispersion of polystyrene particles (Duke Scientific, Part No. 3070A, nominal diameter of 73.0 ± 2.6 nm) which is diluted to 1% w/w such that the interactions between the particles are negligible. A capillary tube with a rectangular section (Vitrocom, Inc.) is filled with the colloidal dispersion and imaged by means of a commercial microscope (LEICA DM IRB). The images are acquired with a complementary metal-oxide-semiconductor (CMOS) camera (IDT X-Stream *XS*-3, 1280×1024 pixels, pixel size of 12 μm). The thickness of the capillary tube along the optical axis is 100 μm and the midplane of the capillary tube is imaged onto the camera sensor. Typical data consist of a sequence of approximately 1000–2000 images, acquired with a sampling rate of 100–400 images/s and with an exposure time of 2.5–10 ms.

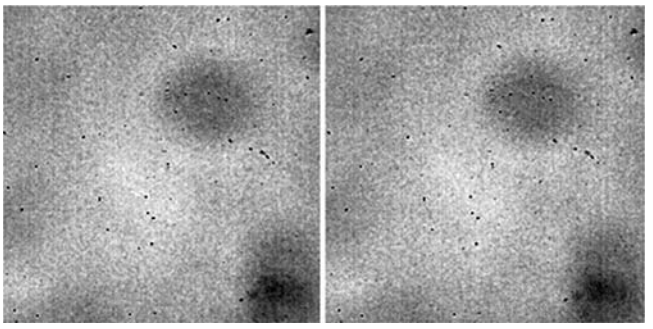

FIG. 1. Microscopy images of a colloidal dispersion acquired 1 s apart in time (details in the text). The size of each panel corresponds to about 150 μm. Because of the small scattering signal of the particles the two images appear to be identical. The visible signal is due mainly to stray light (for example, dust particles on the optical surfaces of the microscope, on the detector, and on the surfaces of the sample cell).

In Fig. 1 we show two images that are obtained at $\Delta t = 1$ s distance with the following experimental parameters: exposure time of 2.5 ms, numerical aperture of the objective $N_o = 0.85$, magnification $M = 40$, 2×2 binning, and effective pixel size $d_{pix} = 0.6$ μm. Both images exhibit a strong background due to the transmitted beam and artifacts due to dust particles on the camera sensor and imperfections on the optical surfaces. The scattering contributions of the particles are barely visible and can be brought to light by selecting the image in Fig. 1 (left) as a reference and subtracting it from the one taken at later time. This procedure is expected to remove all the time-independent signals and to isolate the signal associated with the particles' motion. The subtraction procedure can be repeated for different values of Δt, as shown in Fig. 2. The inspection of Fig. 2 reveals that the time-independent stray signal present in the original images has been effectively removed from the original images. A small-scale signal is now evident which is purely associated with the particles' motion. The amplitude of the signal increases with Δt and a more quantitative assessment of this increase can be obtained by defining the stochastic two-

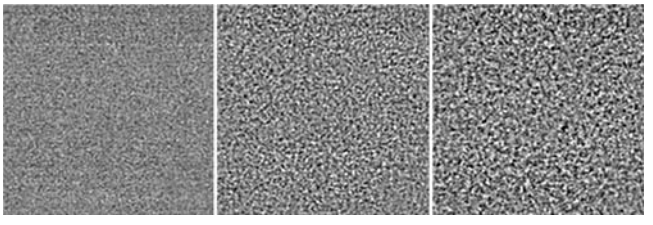

FIG. 2. Images obtained by subtracting two microscopy images that are taken at time intervals of $\Delta t = 0.01$, 0.1, and 1 s (from left to right). The subtraction removes efficiently the stray signal and isolates the contribution due to the particles. The average size of the speckles gives an estimate of the microscope resolution. The contrast in the images increases with Δt.

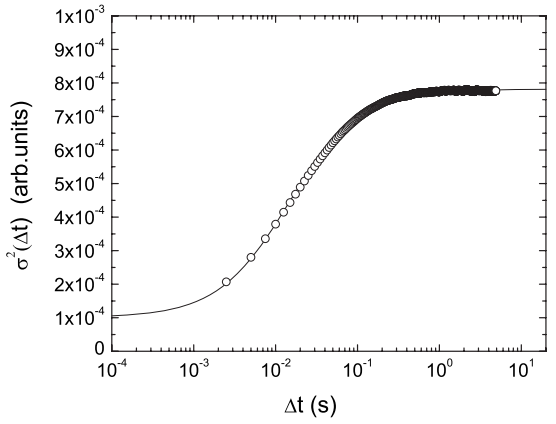

FIG. 3. The particle rearrangement due to their Brownian motion causes an increase in the variance of the intensity fluctuation $\Delta I(\mathbf{x};\Delta t)$. With increasing time delay Δt, the two subtracted images become progressively uncorrelated, such that $\sigma^2(\Delta t)$ saturates at large Δt. Each experimental point is the result of an average obtained by using 100 statistically independent ΔI images with the same Δt. The line is drawn with no adjustable parameters from the theory presented in Sec. III.

dimensional variable $\Delta I(\mathbf{x},t;\Delta t)=I(\mathbf{x},t+\Delta t)-I(\mathbf{x},t)$, where $I(\mathbf{x},t)$ is the intensity detected at the pixel with position $\mathbf{x}$ on the detector.

In the following we will make the simplifying but not necessary assumption that the dynamics is stationary, i.e., the dynamical properties of the system depend only on the time delay Δt but not on the actual time t that is chosen as a reference. We will drop accordingly the dependence on t. The expectation value $\langle \Delta I(\mathbf{x};\Delta t)\rangle$ is then equal to zero and the energy content of the intensity fluctuation $\Delta I(\mathbf{x};\Delta t)$ can be quantified by its first nonzero moment, i.e., the expectation value $\sigma^2(\Delta t)$ of the variance defined as

$$\sigma^2(\Delta t) = \int\int \langle |\Delta I(\mathbf{x};\Delta t)|^2\rangle d\mathbf{x}. \tag{1}$$

For dynamically active systems, $\sigma^2(\Delta t)$ is expected to increase with Δt as a consequence of the particles' motion [19]. For our Brownian colloidal dispersion, this increase is shown in Fig. 3, where we display data obtained with the highest frame rate (400 Hz) to capture the initial increase in the variance. The signal increases from a small background value, associated with the detector noise, and saturates to a plateau, which is indicative of the complete loss of positional correlation between the particles.

The DDM technique is based on a Fourier analysis of $\Delta I(\mathbf{x};\Delta t)$ and the basic concept behind it is easily explained for a 2D object, i.e., for a sample having negligible thickness along the optical axis. The object refractive index distribution can be Fourier decomposed and each Fourier component can be labeled with a 2D Fourier wave vector $\mathbf{q}_{obj}$. Each Fourier component of the refractive index distribution acts as a periodic diffraction grating, scattering light at an angle $\theta=\sin^{-1}(q_{obj}/k_o)$ with respect to the incident wave vector $\mathbf{k}_o$. For an imaging system with unitary magnification, the diffracted plane wave causes in the image a sinusoidal fringe pattern with 2D Fourier wave vector q such that

$$q = 2\pi\frac{\sin\theta}{\lambda_o} = q_{obj}, \tag{2}$$

where we have used $k_o=2\pi/\lambda_o$ (λ_o is the wavelength of light). Equation (2) is the key relation for performing DDM experiments and, more generally, near-field scattering experiments. Indeed, it relates to a one-to-one fashion a Fourier component of the measured intensity distribution with the corresponding one in terms of the sample refractive index.

The simplest way of taking advantage of this result would be to study the behavior in time of the Fourier transform of the intensity $I(\mathbf{x},t)$, defined as $\hat{I}(\mathbf{q},t)=(1/2\pi)\int\int d\mathbf{x}\, I(\mathbf{x},t)e^{-j\mathbf{q}\cdot\mathbf{x}}$, where $\mathbf{q}=(q_x,q_y)$. This could be easily done by means of the *image correlation function*

$$G(\mathbf{q},\Delta t) = \langle \hat{I}^*(\mathbf{q},0)\hat{I}(\mathbf{q},\Delta t)\rangle \tag{3}$$

or the *normalized image correlation function*

$$g(\mathbf{q},\Delta t) = \frac{G(\mathbf{q},\Delta t)}{G(\mathbf{q},0)}. \tag{4}$$

Here, the expectation value $\langle\cdots\rangle$ is taken over many statistically independent realizations of the signal. For the case of Brownian motion considered here, we can calculate the 2D correlation function [4]

$$g_{2D}(\mathbf{q},\Delta t) = \exp[-\Delta t/\tau_d(q)], \tag{5}$$

where $\tau_d(q)=(D_m q^2)^{-1}$ is the characteristic diffusion time constant and D_m is the particle diffusion coefficient. However, because of the large and nonhomogeneous background intensity, it was seminally suggested in Ref. [10] that a more robust statistical estimator is represented by the expectation value of the Fourier power spectrum of $\Delta I(\mathbf{x};\Delta t)$, i.e.,

$$D(\mathbf{q},\Delta t) \doteq \langle |\Delta\hat{I}(\mathbf{q};\Delta t)|^2\rangle. \tag{6}$$

Incidentally $D(\mathbf{q},\Delta t)$ is the two-dimensional generalization of the *photon structure function* used in DLS experiments [21–24]. To stress the fact that the use of images allows us to have a multitude (typically more than 1.0×10^6) of photon structure functions in parallel, we will name it *image structure function*. In analogy with DLS, the correlation and the structure functions are related by

$$D(\mathbf{q},\Delta t) = 2[G(\mathbf{q},0) - G(\mathbf{q},\Delta t)], \tag{7}$$

which is valid for statistically stationary processes. It is worth noting that $G(\mathbf{q},\Delta t)$ is a decreasing function of Δt from $G(\mathbf{q},0)$ to $G(\mathbf{q},\Delta t\to\infty)=0$. Equation (7) implies that $D(\mathbf{q},\Delta t)$ is an increasing function of Δt from zero to $2G(\mathbf{q},0)$. Even if from a theoretical point of view the structure and the correlation functions are equivalent, we will use for the data analysis the structure function approach (a deeper discussion about this point can be found in Sec. V).

Without prior knowledge about the relationship occurring between intensity and refractive index fluctuations, the structure function is generally given by

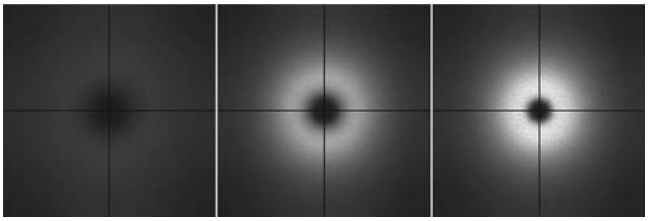

FIG. 4. Experimentally determined image structure function $D(\mathbf{q},\Delta t)$ for the images $\Delta I(\mathbf{x};\Delta t)$ in Fig. 2: Δt=0.01 *s*, Δt=0.1 *s*, and Δt=1 *s*. Each image is the result of an average over 2000 statistically independent ΔI images with the same Δt. The black cross at the center of each image is the result of a postprocessing operation and is used to suppress artificially large contributions due to image processing artifacts. The larger energy content of the right image can be appreciated.

$$D(\mathbf{q},\Delta t) = A(\mathbf{q})[1 - g(\mathbf{q},\Delta t)] + B(\mathbf{q}), \qquad (8)$$

where $A(\mathbf{q})$ is related to the scattering properties of the particles, to the coherence properties of the light source, and to the properties of the microscope objective. $B(\mathbf{q})$ accounts for the noise of the detection system and is equal to 2 times the power spectrum of the camera noise. As already pointed out in Ref. [19], previous knowledge of $A(\mathbf{q})$ and $B(\mathbf{q})$ is not necessary for performing DDM experiments. For example, in the case of Brownian motion, we can use Eq. (5) and treat $A(q)$, $B(q)$, and $\tau_d(q)$ as fitting parameters. The information about the dynamics can then be extracted from the analysis of the parameter $\tau_d(q)$.

In Fig. 4 we show $D(\mathbf{q},\Delta t)$ for different values of Δt. As expected the energy content increases with Δt. Because of the azimuthal symmetry exhibited by $D(\mathbf{q},\Delta t)$, we consider the azimuthal average $D(q,\Delta t)$, where $q=\sqrt{q_x^2+q_y^2}$. The result of this averaging operation is shown in Fig. 5, where the azimuthal average $D(q,\Delta t)$ as a function of the wave vector q is presented for different values of the time delay Δt. The area under the curve, i.e., the variance $\sigma^2(\Delta t)$, increases with Δt.

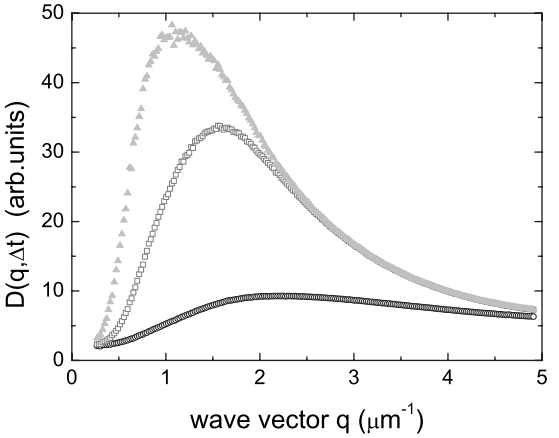

FIG. 5. The image structure function $D(q,\Delta t)$ is plotted as a function of q for different values of Δt: Δt=0.01 s (open circles, black), Δt=0.1 s (open squares, dark gray), and Δt=1 s (close up triangles, light gray).

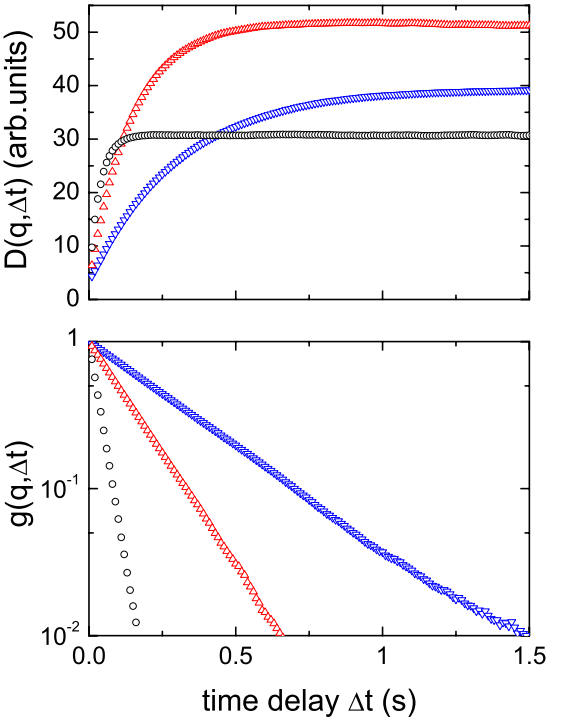

FIG. 6. (Color online) (Top) Growth of $D(q,\Delta t)$ as a function of Δt for three different values of q: 0.70 (blue down triangles), 1.06 (red up triangles), and 2.13 μm^{-1} (black circles). (Bottom) Exponential decay of the normalized correlation function $G(q,\Delta t)$ corresponding to the same wave vectors.

The characterization of the dynamics passes through the analysis of the behavior of $D(q,\Delta t)$ as a function of the time delay Δt. Typical curves are presented in Fig. 6 for different wave vectors q. From a fitting procedure based on Eq. (8), it is possible to extract $A(q)$, $B(q)$, and $\tau_d(q)$. To facilitate the comparison with DLS experiments, we plot in Fig. 6 (bottom panel) the normalized correlation function $g(q,\Delta t)=1-[D(q,\Delta t)-B(q)]/A(q)$. A fair exponential decay is observed for the three data sets, as expected for a Brownian system.

The results of the fitting procedure for $\tau_d(q)$ are plotted in Fig. 7 (open symbols), together with data points obtained with a traditional rotating-arm DLS setup (closed symbols). The DLS data have been acquired on a more dilute sample (0.001% w/w) in the angular range of 20°–150°. The two data sets agree very satisfactorily with the predictions of the Stokes-Einstein-Sutherland relation $D_m=k_BT/(6\pi\eta R)$. Here, k_B is the Boltzmann constant, T is the absolute temperature, η is the solvent viscosity, and $2R$ is the particle diameter. The result of the theoretical estimate, accounting for the polydispersity of the sample and including a correction for the finite concentration of the colloids is $D_m=6.0\pm0.2$ μm^2/s, in good agreement with the experimental data. Figure 7 shows that DDM operates at extremely low q, typically not accessible with DLS and that the simultaneous use of the two techniques guarantees an access to dynamical information over more than 2 decades in q.

As far as the other two fitting parameters are concerned, we show in Fig. 8 the results for the amplitude $A(q)$ and the

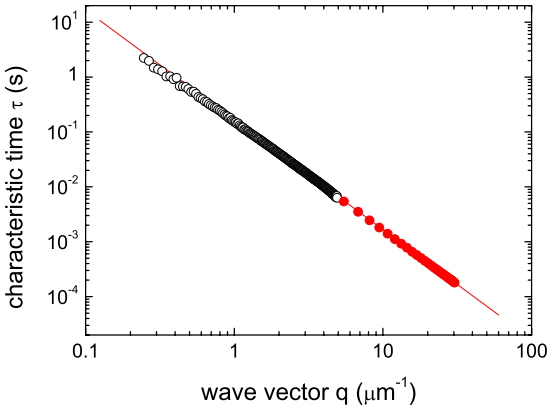

FIG. 7. (Color online) Experimentally determined characteristic decay time τ_d plotted against the wave vector q for the 73 nm particles. Open (black) circles are data obtained with DDM. Close (red) circles are DLS data. The continuous line in the graph is the theoretical estimate corresponding to D_m=6.0 μm^2/s (see text for details).

background $B(q)$ in the wave-vector range $[0.1,5]$ μm^{-1}. The signal $A(q)$ can be appreciably discriminated from the background $B(q)$ in the wave-vector range $[0.3,5]$ μm^{-1}. The function $A(q)$ has a deep minimum at q=0, increases to a peak for $q \simeq 1$ μm^{-1}, and decreases again for larger values of q. Unfortunately, the 2D model presented in Ref. [19] and outlined above cannot quantitatively account for the behavior of $A(q)$. In this paper we derive a 3D theory that, among other things, predicts the behavior of $A(q)$ as a function of the parameters of the microscope. We anticipate here that the theory captures the basic ingredients of the experiments as can be appreciated from Fig. 8, where the result of the fitting of the $A(q)$ data with Eq. (62) is shown as a dashed line. The agreement of the data with the theory is good and will be discussed in more detail in Sec. III.

A. Toward a 3D model: The Brownian particle

Let us consider a Rayleigh scatterer, i.e., a particle whose size is much smaller than the wavelength λ_0 and a mono-

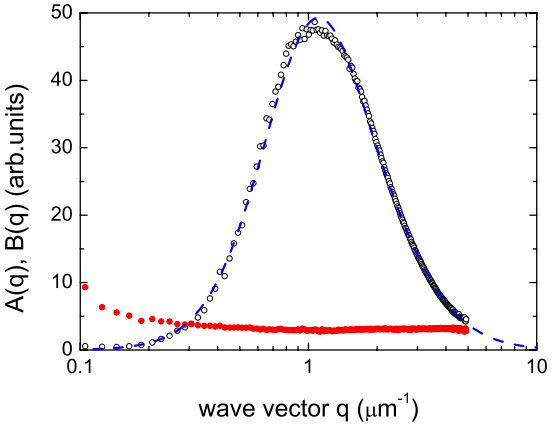

FIG. 8. (Color online) Experimentally determined $A(q)$,$B(q)$ plotted against the wave vector q for a colloidal dispersion of particles with a diameter of 73 nm. The dashed line is a fit of the data for $A(q)$ as discussed in the text.

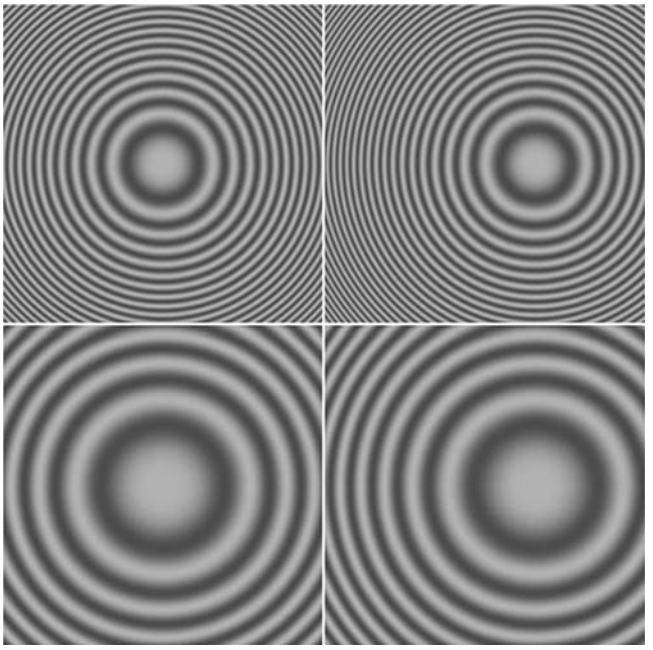

FIG. 9. Simulated interference pattern generated at some distance from a Rayleigh scatterer (particle) illuminated by a plane wave, which propagates along the z direction. (Upper left) the particle is in (x_0,y_0,z_0); (upper right) the particle has moved in $(x_0+\Delta x, y_0+\Delta y, z_0)$. The fringes are unchanged and translated in the (x,y) plane by an amount $(\Delta x,\Delta y)$; (lower left) the particle is in $(x_0,y_0,z_0+\Delta z)$ i.e., further away from the image plane. The fringes are not translated in the (x,y) plane but their shape has changed; (lower right) the particle is in $(x_0+\Delta x, y_0+\Delta y, z_0+\Delta z)$. The fringes are translated in the (x,y) plane by an amount $(\Delta x,\Delta y)$ and also modified by virtue of the particle axial displacement Δz.

chromatic plane wave $e^{jk_0 z}$ impinging on the particle along the optical axis z. The unitary amplitude impinging plane wave is characterized by a wave vector $\mathbf{k}_i$ and the light quasielastically scattered at an angle θ with respect to the incident direction has a wave vector $\mathbf{k}_s$, where $k_0=|\mathbf{k}_s|=|\mathbf{k}_i|$ (see Fig. 10 for the wave-vector diagram). The interaction of the particle with the plane wave produces a spherical wave propagating away from the particle and centered on it [25]. The resulting scalar field, measured at distance z from the particle center, is given by

$$U(\mathbf{x},z) = e^{jk_0 z} + S\frac{e^{jk_0 r}}{r}, \tag{9}$$

where $r=\sqrt{|\mathbf{x}|^2+z^2}$ and S is related to the scattering contrast of the particle [25]. With a simple change in the reference frame, we can write the intensity pattern in the plane z=0 due to a particle located in $(\mathbf{x}_0,z_0)$ as

$$I(\mathbf{x}|\mathbf{x}_0,z_0) \simeq 1 + \frac{2S}{z_0}\cos\left(\frac{k_0|\mathbf{x}-\mathbf{x}_0|^2}{2z_0}\right), \tag{10}$$

where we made the paraxial approximation $r=\sqrt{|\mathbf{x}|^2+z^2}\simeq z+|\mathbf{x}|^2/2z$. This pattern has the typical appearance shown in Fig. 9, where it can be appreciated that, while a particle displacement in the (x,y) plane causes an overall translation of the fringes, a motion along z is associated with a change in

the fringe spacing, which depends on the value of z_0. These fringes do contain precious information about the position of the particles along the optical axis z. In principle this information allows for the recovery of the three-dimensional position of the particle as routinely done in digital holographic microscopy [26].

Here, we use this information in a different way. The two-dimensional Fourier transform of the intensity pattern is given by

$$\hat{I}(\mathbf{q}|\mathbf{x}_0,z_0) \simeq \delta(\mathbf{q}) + \frac{2S}{k_0} e^{j\mathbf{q}\cdot\mathbf{x}_0} \sin(q_z z_0) \tag{11}$$

where $q_z \simeq q^2/2k_0$ is the paraxial approximation of the z component of the scattering wave vector $\mathbf{Q}=\mathbf{k}_s-\mathbf{k}_i=(\mathbf{q},q_z)$. Indeed, $Q=|\mathbf{Q}|=2k_0 \sin(\theta/2) \simeq k_0\theta$,

$$Q^2 \simeq q^2 + \left(\frac{q^2}{2k_0}\right)^2, \tag{12}$$

which implies that $q_z \simeq q^2/2k_0$.

It has to be noted that results similar to Eq. (11) have been already presented before [27–30] for visible, x-ray, and electron optics. The single-particle model used here allows us to easily interpret in the Fourier space any particle motions. The motion of the particle along the z axis causes an appreciable phase shift of $\hat{I}(\mathbf{q})$ when an axial displacement on the order of $1/q_z$ takes place, whereas a displacement in the transverse plane has to be on the order of $1/q$ to cause an appreciable effect. By assuming a Brownian motion of the particle with a diffusion coefficient D_m and inserting the above expression in Eq. (6), we obtain

$$\begin{aligned} D(\mathbf{q},\Delta t) &= 2G(\mathbf{q},0)[1-e^{-D_m(q^2+q_z^2)\Delta t}] \\ &= 2G(\mathbf{q},0)(1-e^{-D_m Q^2 \Delta t}), \end{aligned} \tag{13}$$

where $G(\mathbf{q},0)=4S^2/k_0^2$. This model can be easily extended to a collection of noninteracting identical particles and one obtains a result identical to Eq. (13). This result shows that the dynamics of the Brownian motion of a system of particles can be characterized by investigating the image structure function. The outcome of this investigation performed with coherent light is fully equivalent to a DLS experiment, provided that the dynamics measured at the 2D wave vector q is correctly associated with the correct 3D wave vector Q. It is worth noting that for small scattering angles θ one has $Q \simeq q$ and the fractional error in the determination of the characteristic time of the exponential by assuming that $Q \simeq q$ scales as $(Q/2k_0)^2=\sin^2(\theta/2)$. For example for $\theta \simeq 20°$ the fractional error amounts to about 3%. The advantage of the single-particle model is that it can be easily used to get a semiquantitative understanding of the effects of the limited coherence of the illuminating light. To this purpose we draw in Figs. 11 and 12 two wave-vector diagrams similar to the one reported in Fig. 10 for plane-wave illumination. These diagrams illustrate the main effect of partially coherent illumination on a scattering experiment: different three-dimensional wave vectors $\mathbf{Q}$ may give rise to the same two-dimensional projection $\mathbf{q}$.

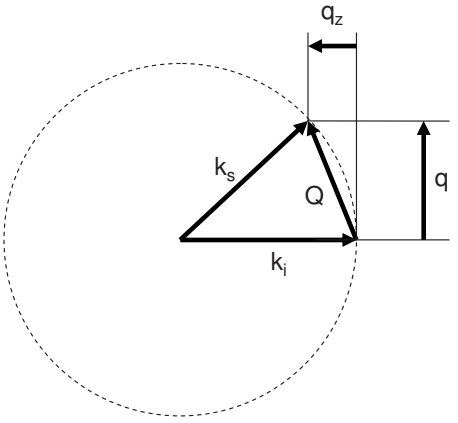

FIG. 10. Diagram showing the relationship between the wave vectors involved in the scattering and imaging processes. The reference system is chosen as follows. The z axis coincides with the direction of propagation of the incident light, which is characterized by the wave vector $\mathbf{k}_i$. The (x,y) plane is perpendicular to the incident wave vector.

In the case of spatially incoherent illumination the particle is illuminated with a set of plane waves whose mutual phase relationship is a random stochastic variable. In Fig. 11 we can appreciate that the wave vector $\mathbf{k}_1$ gives rise to a scattering wave vector $\mathbf{Q}_1=(\mathbf{q}_1,q_{z_1})$ and $\mathbf{k}_2$ to a scattering wave vector $\mathbf{Q}_2=(\mathbf{q}_2,q_{z_2})$. The two wave vectors $\mathbf{q}_1$ and $\mathbf{q}_2$ can have the same amplitude provided that the z components have the appropriate value. This means that the two-dimensional wave vector $\mathbf{q}$ might correspond to different three-dimensional wave vectors $\mathbf{Q}$.

A similar effect can be associated with the polychromaticity of the source. In Fig. 12 the two wave vectors $\mathbf{k}_1$ and $\mathbf{k}_2$ do not differ in direction, as for the previous case, but in amplitude, due to their different wavelengths. Again, the one-to-one correspondence between $\mathbf{q}$ and $\mathbf{Q}$ is lost. In general for every $\mathbf{q}$ it exists a whole set of q_z that correspond to the same three-dimensional wave vector $\mathbf{Q}$.

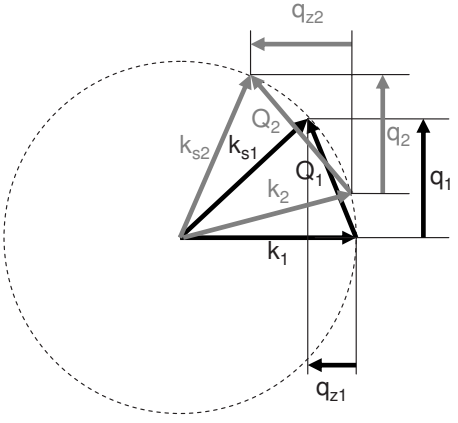

FIG. 11. Two plane waves forming different angles with respect to the optical axis are characterized by two wave vectors $\mathbf{k}_1$ and $\mathbf{k}_2$ with the same amplitude k but different directions. They give rise to the same two-dimensional projection $\mathbf{q}$, provided that the components $\mathbf{q}_{z1}$ and $\mathbf{q}_{z2}$ are different. Therefore, we expect $\Delta q \neq 0$ whenever $N_s \neq 0$.

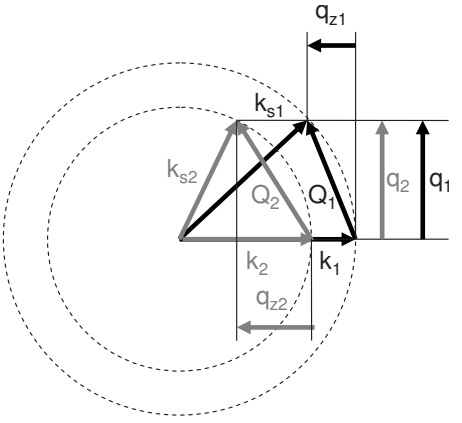

FIG. 12. Two plane waves having different wavelengths are characterized by two wave vectors $\mathbf{k}_1$ and $\mathbf{k}_2$ with different amplitudes but with the same direction. If they impinge on the sample along the same direction, they could give rise to the same two-dimensional projection $\mathbf{q}$, provided that the components $\mathbf{q}_{z1}$ and $\mathbf{q}_{z2}$ are different. Therefore, we expect $\Delta q \neq 0$ whenever $\Delta\lambda \neq 0$.

B. Lack of spatial coherence

We model the lack of spatial coherence by assuming that the illuminating beam is the (incoherent) superposition of many monochromatic plane waves of the form $U_{\delta\mathbf{k}} = e^{jk_0 z + \delta\mathbf{k}\cdot\mathbf{x}}$. Such a wave forms an angle $\delta k/k_0$ with respect to the z axis. The summation over the intensity pattern associated with each independent plane wave leads to

$$I(\mathbf{x}|\mathbf{x}_0,z_0) \simeq 1 + \frac{2S}{z_0}\left\langle \cos\left(\frac{k|\mathbf{x}-\mathbf{x}_0|^2}{2z_0} - \delta\mathbf{k}\cdot(\mathbf{x}-\mathbf{x}_0)\right)\right\rangle_{\delta\mathbf{k}} = 1 + \frac{2S}{z_0}\hat{f}[\Delta k_s(\mathbf{x}-\mathbf{x}_0)]\cos\left(\frac{k|\mathbf{x}-\mathbf{x}_0|^2}{2z_0}\right), \quad (14)$$

where we have used as a weight function $P(\delta\mathbf{k}) = (1/\Delta k_s^2) f(\delta\mathbf{k}/\Delta k_s)$, and where f is assumed to be a normalized symmetric bell-shaped function with width of ~ 1. In this model $\Delta k_s/k_0 \simeq 2N_s$, where N_s indicates the numerical aperture of the source. This expression leads to a Fourier intensity pattern

$$\hat{I}(\mathbf{q}|\mathbf{x}_0,z_0) \simeq \delta(\mathbf{q}) + \frac{2S}{k_0} e^{j\mathbf{q}\cdot\mathbf{x}_0} f(\mathbf{q}/\Delta k_s) \otimes_{\mathbf{q}} \sin(\bar{q}_z z_0), \quad (15)$$

where the symbol $\otimes_{\mathbf{q}}$ indicates a convolution operation with respect to the variable $\mathbf{q}$. Interestingly, the loss of spatial coherence does not affect the transverse part of $\hat{I}(\mathbf{q}|\mathbf{x}_0,z_0)$ but only the z-dependent term. The function $\sin(\bar{q}_z z_0) = \sin(\frac{q^2 z_0}{2k_0})$ is a chirped function of q, whose local spatial frequency scales as qz_0/k_0. This implies that the convolution operation leaves the function $\sin(\bar{q}_z z_0)$ more or less unchanged at small wave vectors q, where the width of $f(\mathbf{q}/\Delta k_s)$ remains small with respect to the local spatial period of $\sin(\bar{q}_z z_0)$. For large q the oscillations of $\sin(\bar{q}_z z_0)$ are smeared out and average to zero. The crossover value of z_0 that marks this transition is

$$L_s = \frac{k_0}{q\Delta k_s} = \frac{1}{2qN_s}. \quad (16)$$

This value can be interpreted as a q-dependent depth of focus and should be compared with the typical distance traveled by a particle during a time interval Δt. If

$$\Delta t \ll \tau_s \sim \frac{L_s^2}{D_m} \simeq \frac{1}{(N_s)^2 D_m q^2}, \quad (17)$$

the dynamics is not affected by the limited spatial coherence of the light. For longer times the path becomes longer than L_s and this imposes a cutoff on the structure function. By taking into account that the Brownian motion acts on time scale on the order of $1/D_m q^2$, the condition for neglecting this spurious dynamics becomes

$$N_s \ll 1, \quad (18)$$

i.e., as expected the numerical aperture of the light source should be kept small. However, it is worth stressing that the lack of spatial coherence introduces a q-independent effect. Minimizing the effect of the illumination numerical aperture at one wave vector guarantees that the correct dynamics is measured at every wave vector. Equation (18) can be made more quantitative by providing a detailed expression for $f(\mathbf{q}/\Delta k_s)$. At this stage this is not worth in view of the complete model that will be presented in Sec. III.

C. Lack of temporal coherence

A similar reasoning can be made for describing the effect of the limited temporal coherence that can be modeled by assuming that the illuminating beam is the (incoherent) superposition of many monochromatic plane waves with different wavelengths (wave vectors) $U_{\delta\mathbf{k}} = e^{j(k_0+\delta k)z}$. We can again assume a spread $P(\delta k) = (1/\Delta k_t) g(\delta k/\Delta k_t)$, where g is again assumed to be a normalized symmetric bell-shaped function of unitary width. Under this assumption,

$$\hat{I}(\mathbf{q}|\mathbf{x}_0,z_0) \simeq \delta(\mathbf{q}) + \frac{2S}{k_0} e^{j\mathbf{q}\cdot\mathbf{x}_0}\left\langle \sin\left[\bar{q}_z\left(1-\frac{\delta k}{k_0}\right)z_0\right]\right\rangle_{\delta k} = \delta(\mathbf{q}) + \frac{2S}{k_0} e^{j\mathbf{q}\cdot\mathbf{x}_0}\hat{g}\left(\frac{\Delta k_t}{k_0}\bar{q}_z z_0\right)\sin(\bar{q}_z z_0), \quad (19)$$

where $\hat{g}$ is the Fourier transform of the spectral distribution g. By following a line of reasoning similar to the one outlined above for the case of limited spatial coherence, it is possible to identify a q-dependent depth of focus

$$L_t = \frac{k_0}{\bar{q}_z \Delta k_t}. \quad (20)$$

In this case if

$$\Delta t \ll \tau_t \sim \frac{L_t^2}{D_m} = \left(\frac{k_0}{\Delta k_t}\right)^2 \frac{1}{D_m \bar{q}_z^2}, \quad (21)$$

the effect of the limited temporal coherence of the source can be neglected. Again, we can compare τ_m with the Brownian time scale and we get the condition

$$q \ll \frac{1}{\Delta\lambda} \tag{22}$$

for neglecting the spurious dynamics across L_t. By contrast with the previous case we find a q-dependent condition. An order of magnitude estimate can be obtained by considering that for typical microscope lamps one has $\Delta\lambda \simeq 0.1$ μm and Eq. (22) becomes $q \ll 10$ μm^{-1}. Again, a more precise estimate would require to model the function $P(\delta k)=(1/\Delta k_t)g(\delta k/\Delta k_t)$, which is not done in this section.

The single-particle model just presented succeeds in pointing out the basic ingredients of the effect of partially coherent illumination in dynamic microscopy experiments. In the next section we will use a more general approach based on Fourier optics arguments. This approach is valid for an arbitrary refractive index distribution of the (weak) object and accounts also for the properties of the collection optics.

III. MICROSCOPY OF WEAK OBJECTS

A. Nemoto-Streibl model of a microscope

An elegant but rather involved treatment of quasimonochromatic (i.e., the wavelength spread $\Delta\lambda$ is negligible with respect to the peak wavelength λ_0) microscopy with partially coherent light has been proposed by Streibl for 3D weakly scattering objects [31]. The description is based on the Helmholtz equation for the scalar field $U(\mathbf{x})$ and the object is assumed to be weak in such a way to allow for a first-order Born approximation. A subsequent theory due to Nemoto [32] succeeded in showing that Streibl description is consistent with the well-known theory of 2D image formation due to Hopkins [33,34]. If each layer within the object is treated independently with the Hopkins theory, the final image is shown by Nemoto to coincide with the sum of the images of the individual layers. We find convenient to rewrite the Nemoto-Streibl results in the following way:

$$I(\mathbf{x},t) = I_0 + \int\int\int d\mathbf{x}'dz'\ K(\mathbf{x}-\mathbf{x}',-z')c(\mathbf{x}',z',t). \tag{23}$$

This means that the intensity in the image plane is a linear superposition of all the contributions coming from the different layers of the object. Each of these contributions is a $\mathbf{x}$ convolution of the density $c(\mathbf{x},z,t)$ with the transfer function $K(\mathbf{x},z)$ that also acts as a weighting function along z. The model of the kernel $K(\mathbf{x},z)$ is a challenging task and we report here the results of Nemoto, by using a notation more suitable to our purposes.

The layout of the microscope is presented in Fig. 13 that describes a 6-f imaging system characterized by unitary magnification. The light emitted by a light source with intensity $S(\mathbf{q})$ is sent onto the object by using a condenser lens. The object is described by a complex transmission function $f(\mathbf{x},z)=|f(\mathbf{x},z)|\exp[j\phi(\mathbf{x},z)]$. If the object is weak [i.e., if $|f(\mathbf{x},z)|\simeq 1$ and $\phi(\mathbf{x},z)\simeq 0$], one has $f(\mathbf{x},z)=1+f_A(\mathbf{x},z)+jf_P(\mathbf{x},z)$, where $|f_A(\mathbf{x},z)|\ll 1$ and $f_P(\mathbf{x},z)\simeq\phi(\mathbf{x},z)$. Our object can be generally described in terms of the density $c(\mathbf{x},z,t)$ of the moving particles, where t indicates time, z

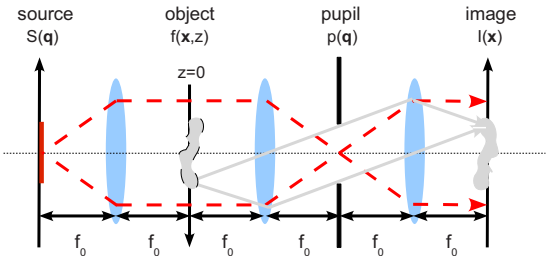

FIG. 13. (Color online) Simplified layout of an optical microscope.

tags the particles' position along the optical axis, and $\mathbf{x}=(x,y)$ is perpendicular to it. The coefficients a_A and a_P are strictly related to the complex refractive index $n=n_R+jn_I$ because $f(\mathbf{x},z)=1+f_A(\mathbf{x},z)+jf_P(\mathbf{x},z)=1+jk_0\frac{\partial n}{\partial c}c(\mathbf{x},z)$. This implies the relations $f_A=a_Ac(\mathbf{x},z)$ and $f_P=a_Pc(\mathbf{x},z)$. It is evident from Fig. 13 that the object is extended along the optical axis z and that the plane $z=0$ is located somewhere in its proximity. Also, we will temporarily assume that the sample thickness along z is infinite. The light scattered by the object recombines with the transmitted beam onto a suitable sensor (typically a pixel detector) by means of an optical system (objective) described by a pupil function $p(\mathbf{q})$. It is worth noting that the function $S(\mathbf{q})$ is directly related to the *mutual coherence function* in the object plane $j_S(\mathbf{r})=\langle U_0(\mathbf{x}+\mathbf{r})U_0^*(\mathbf{x})\rangle$, where $U_0(\mathbf{x})\equiv U(\mathbf{x},z=0)$. The link between the two functions is given by the Van Cittert and Zernike theorem [34] that is easily expressed in the following form:

$$J_S(\mathbf{q}) = S(\mathbf{q}), \tag{24}$$

where $J_S(\mathbf{q})$ is the 2D FT of $j_S(\mathbf{r})$.

Under the reasonable assumption that both $J_S(\mathbf{q})$ and $p(\mathbf{q})$ are real-valued functions we obtain

$$\tilde{K}(\mathbf{q},q_z) = a_AT_{AF}(\mathbf{q},q_z) + ja_PT_{PF}(\mathbf{q},q_z), \tag{25}$$

where

$$\begin{pmatrix} T_{AF}(\mathbf{q},q_z) \\ T_{PF}(\mathbf{q},q_z) \end{pmatrix} = T_+(\mathbf{q},q_z) \pm T_-(\mathbf{q},q_z) \tag{26}$$

and

$$T_\pm(\mathbf{q},q_z) \equiv \int\int p^*\left(\mathbf{q}'+\frac{\mathbf{q}}{2}\right)J_S\left(\mathbf{q}'\pm\frac{\mathbf{q}}{2}\right)p\left(\mathbf{q}'-\frac{\mathbf{q}}{2}\right)\delta\left(q_z + \frac{\mathbf{q}\cdot\mathbf{q}'}{k_0}\right)d\mathbf{q}'. \tag{27}$$

In Eq. (25) we have introduced the 3D Fourier transform $\tilde{K}(\mathbf{Q})=(2\pi)^{-3/2}\int\int\int d\mathbf{X}\ K(\mathbf{X})e^{-j\mathbf{Q}\cdot\mathbf{X}}$, where $\mathbf{X}=(\mathbf{x},z)$ and $\mathbf{Q}=(\mathbf{q},q_z)$. The two functions $T_{AF}(\mathbf{q},q_z)$ and $T_{PF}(\mathbf{q},q_z)$ are 3D optical transfer functions (OTFs), respectively, for the amplitude and the phase of the object. They account for the partial coherence of the light source, the properties of the objective, and the 3D nature of the object.

If we assume in addition that both $J_S(\mathbf{q})$ and $p(\mathbf{q})$ are even functions we can write

$$\begin{pmatrix} T_{AF}(\mathbf{q},q_z) \\ T_{PF}(\mathbf{q},q_z) \end{pmatrix} = T(\mathbf{q},q_z) \pm T(\mathbf{q},-q_z), \tag{28}$$

where we have reduced the knowledge of the two functions T_{AF} and T_{PF} to the knowledge of the single function $T(\mathbf{q},q_z) \equiv T_+(\mathbf{q},q_z)$, which is also an even function with respect to $\mathbf{q}$. The evenness of $J_S(\mathbf{q})$ and $p(\mathbf{q})$ is very plausible in most cases. Indeed, the typical apertures in microscopes are described by circularly symmetric functions and the angular distribution of light from the source does also exhibit a symmetric nature.

B. Calculation of the transfer function $T(\mathbf{q},q_z)$

An analytical calculation of the transfer function $T(\mathbf{q},q_z)$ is a challenging task for realistic pupils and sources. A numerical analysis of the imaging problem can be performed by using the formulas derived here. However, such an analysis is outside the aim of the present work, in which we prefer to describe the basic physics of the imaging problem by using convenient Gaussian functions in both cases. This allows us to obtain exact results to guide the experimentalists in choosing optimum working conditions for dynamic microscopy experiments.

We model the source coherence with

$$J_S(\mathbf{q}) = \frac{1}{2\pi\sigma_c^2 k_0^2}\exp\left(-\frac{1}{2}\frac{q^2}{\sigma_c^2 k_0^2}\right) \tag{29}$$

and the pupil function with

$$p(\mathbf{q}) = \exp\left(-\frac{1}{2}\frac{q^2}{\sigma_o^2 k_0^2}\right), \tag{30}$$

where σ_c gives an estimate of the numerical aperture of the condenser and σ_o of the objective. We define the *incoherence parameter*

$$M = \frac{\sigma_c}{\sigma_o} \tag{31}$$

that allows a continuous transition from spatially coherent ($M=0$) to incoherent ($M=\infty$) illumination. This is consistent with the Hopkins 2D theory of image formation [33], where a similar parameter is used.

By inserting Eqs. (29) and (30) into Eq. (27), we obtain

$$T(\mathbf{q},q_z) = \frac{C(\mathbf{q})}{\sqrt{2\pi}\Delta q(\mathbf{q})}\exp\left[-\frac{1}{2}\left(\frac{q_z-\bar{q}_z(\mathbf{q})}{\Delta q(\mathbf{q})}\right)^2\right]. \tag{32}$$

This function is a Gaussian function of the variable q_z, centered at

$$\bar{q}_z(\mathbf{q}) = \frac{q^2}{2k_0}\left(\frac{1}{1+2M^2}\right) \tag{33}$$

and characterized by a width Δq given by

$$\Delta q^2(\mathbf{q}) = q^2\sigma^2, \tag{34}$$

where

$$\sigma^2 = \frac{1}{\frac{2}{\sigma_o^2}+\frac{1}{\sigma_c^2}} = \frac{\sigma_c^2}{1+2M^2}. \tag{35}$$

Note that $\sigma \simeq \sigma_c$ if $M \ll 1$, while $\sigma \simeq 0$ when $M \gg 1$. The normalization of Eq. (32) is such that $\int T(\mathbf{q},q_z)dq_z = C(\mathbf{q})$, where

$$C(\mathbf{q}) = \frac{\exp\left[-\frac{1}{2}\left(\frac{q}{q_{ro}}\right)^2\right]}{1+2M^2} \tag{36}$$

is a decreasing function of the wave vector q that describes the overall frequency modulation introduced by the imaging process. The decrease in $C(\mathbf{q})$ is characterized by the roll-off wave vector

$$q_{ro} = k_0\sigma_o\sqrt{\frac{1+2M^2}{1+M^2}} \tag{37}$$

that is a measure of the resolution of the microscope. Indeed, the minimum detail that can be resolved by such a microscope is given by

$$x_{\min} = \frac{2\pi}{q_{ro}} = \sqrt{\frac{1+M^2}{1+2M^2}}\frac{\lambda_0}{\sigma_o}. \tag{38}$$

It is quite interesting to note that the resolution increases with the incoherence parameter M in agreement with Hopkins theory for 2D microscopy [33]. More in detail $x_{\min} \to \lambda_0/\sigma_o$ for $M \to 0$ and $x_{\min} \to \lambda_0/(\sqrt{2}\sigma_o)$ for $M \to \infty$. The appearance of the factor $\sqrt{2}$ is a consequence of the choice of Gaussian functions to model the microscope properties. Other choices would lead to different numerical factors but always larger than 1.

As far as the contrast of the microscope images is concerned, we investigate also the behavior of the amplitude and phase transfer functions in Eq. (25). While $T_{AF}(\mathbf{q},q_z)$ is proportional to the sum of two Gaussian functions centered at $\pm\bar{q}_z$, $T_{PF}(\mathbf{q},q_z)$ turns out to be proportional to their difference. The superposition ratio

$$r_s(\mathbf{q}) = \left(\frac{\Delta q}{\bar{q}_z}\right)^2 = \left[2\sigma\frac{k_0}{q}(1+2M^2)\right]^2 \tag{39}$$

is a quantitative measure of the superposition of the two Gaussian functions. If the ratio r_s is small, this superposition is negligible. This happens if $q/k_0 \gg 2\sigma(1+2M^2)$. Only for small M it is possible to satisfy the latter condition together with the requirement that the ray is transmitted through the objective ($q/k_0 \ll \sigma_o$). In this case r_s is small if $q/k_0 \gg \sigma_c$.

Equation (32) is an analytical model for describing 3D microscopy of weak objects. In the context of our paper it will serve as a starting point for a more refined description, incorporating also the effect of polychromatic illumination.

C. Effect of polychromatic illumination

The Streibl-Nemoto theory specified to Gaussian pupil and Gaussian mutual coherence function was used in the previous paragraph for the calculation of the transfer func-

tion $T(\mathbf{q},q_z)$. In this paragraph we shall include the effect of polychromatic illumination. The latter can be accounted for quantitatively by modeling the source with a Gaussian spectrum

$$P(\lambda)=\frac{1}{\sqrt{2\pi}\Delta\lambda}\exp\left[-\frac{1}{2}\frac{(\lambda-\lambda_0)^2}{\Delta\lambda^2}\right] \tag{40}$$

that can be used as a weight function for the individual intensity patterns associated with each wavelength. Again this choice is made in order to obtain results in a closed form. The result of this calculation for the function $T(\mathbf{q},q_z)$ can be still written as in Eq. (32). The most general form for the parameters $\bar{q}_z(\mathbf{q})$, $\Delta q^2(\mathbf{q})$, and $C(\mathbf{q})$ is not particularly useful in this context. Here, we report the simpler approximate expressions obtained with a lowest-order expansion in both M and $\Delta\lambda/\lambda_0$,

$$\bar{q}_z(\mathbf{q})=\frac{q^2}{2k_o}\left[1-2M^2-\frac{1}{\sigma_o^2}\left(\frac{q}{k_0}\right)^2\left(\frac{\Delta\lambda}{\lambda_0}\right)^2\right], \tag{41}$$

$$\Delta q^2(\mathbf{q})=q^2\left[(\sigma_o M)^2+\frac{1}{4}\left(\frac{q}{k_0}\right)^2\left(\frac{\Delta\lambda}{\lambda_0}\right)^2\right], \tag{42}$$

$$C(\mathbf{q})=\frac{\exp\left[-\frac{1}{2}\frac{(q/q_{ro})^2}{1+(q/q_{ro})^2(\Delta\lambda/\lambda_0)^2}\right]}{\sqrt{1+\left(\frac{q}{q_{ro}}\right)^2\left(\frac{\Delta\lambda}{\lambda_0}\right)^2}}, \tag{43}$$

and the result for the superposition ratio reads

$$r_s(\mathbf{q})=4\left(\frac{k_0}{q}\right)^2(\sigma_o M)^2+\left(\frac{\Delta\lambda}{\lambda_0}\right)^2. \tag{44}$$

As a by-product of the lowest-order approximation just made, most of the parameters characterizing $T(\mathbf{q},q_z)$ are expressed as a sum of the contributions due to effects of temporal and spatial coherence limitations, considered separately. It is worth pointing out that the function $P(\lambda)$ shall in principle account also for the effect of the spectral sensitivity of the detectors used, whose effect is to weight the spectral intensity components of the image.

D. Application to Brownian motion

One of the advantages of the 3D model is that the intensity in the microscope images can be quantitatively linked to the sample properties. As far as dynamics is concerned, one has

$$G(\mathbf{q},\Delta t)=\int dq_z|\widetilde{K}(\mathbf{q},q_z)|^2\widetilde{F}(\mathbf{q},q_z,\Delta t), \tag{45}$$

where

$$\widetilde{F}(\mathbf{q},q_z,\Delta t)=\langle\widetilde{c}^*(\mathbf{q},q_z,0)\widetilde{c}(\mathbf{q},q_z,\Delta t)\rangle \tag{46}$$

is the *intermediate scattering function* [35], which is the spatial 3D Fourier transform of the *space-time density-density correlation function*

$$F(\Delta\mathbf{x},\Delta z,\Delta t)\doteq\langle c(0,0,0)c(\Delta\mathbf{x},\Delta z,\Delta t)\rangle. \tag{47}$$

The function $\widetilde{F}(\mathbf{Q},\Delta t)$ has been the object of intense theoretical work in the past and it has been calculated for many cases of practical interest such as, for example, that of colloidal particles undergoing Brownian motion or drifting with uniform velocity [4]. For the Brownian motion of small *noninteracting* particles in a host molecular solvent, $\widetilde{F}(\mathbf{q},q_z,\Delta t)=F_0e^{-D_m(q^2+q_z^2)\Delta t}$ [4] and one obtains

$$G(\mathbf{q},\Delta t)=F_0e^{-D_mq^2\Delta t}\int dq_z|\widetilde{K}(\mathbf{q},q_z)|^2e^{-D_mq_z^2\Delta t} \tag{48}$$

for the correlation function and

$$g(\mathbf{q},\Delta t)=\frac{e^{-D_mq^2\Delta t}\int dq_z|\widetilde{K}(\mathbf{q},q_z)|^2e^{-D_mq_z^2\Delta t}}{\int dq_z|\widetilde{K}(\mathbf{q},q_z)|^2} \tag{49}$$

for the normalized correlation function. By inserting Eqs. (25), (28), and (32) in Eq. (49), we obtain

$$g_P(\mathbf{q},\Delta t)=\frac{e^{-D_mq^2\Delta t}}{\sqrt{1+D_m\Delta t\Delta q^2}}\frac{e^{-[D_m\Delta t/(1+D_m\Delta t\Delta q^2)]\bar{q}_z^2}-e^{-(\bar{q}_z/\Delta q)^2}}{1-e^{-(\bar{q}_z/\Delta q)^2}}, \tag{50}$$

which is valid for phase objects (n_I=0), and

$$g_A(\mathbf{q},\Delta t)=\frac{e^{-D_mq^2\Delta t}}{\sqrt{1+D_m\Delta t\Delta q^2}}\frac{e^{-[D_m\Delta t/(1+D_m\Delta t\Delta q^2)]\bar{q}_z^2}+e^{-(\bar{q}_z/\Delta q)^2}}{1+e^{-(\bar{q}_z/\Delta q)^2}} \tag{51}$$

for amplitude (absorbing) objects (n_R=0). Equations (50) and (51) simplify if the superposition parameter $r_s\ll1$, i.e., if $\Delta q\ll\bar{q}_z$, and in both cases we obtain the 3D generalization of Eq. (5),

$$g(\mathbf{q},\Delta t)\simeq g_{2D}(\mathbf{q},\Delta t)g_z(\mathbf{q},\Delta t), \tag{52}$$

where the factor

$$g_z(\mathbf{q},\Delta t)=\frac{e^{-[D_m\Delta t/(1+\Delta t/\tau_{\Delta q})]\bar{q}_z^2(\mathbf{q})}}{\sqrt{1+\Delta t/\tau_{\Delta q}}} \tag{53}$$

quantifies the contribution of the particles' motion along the microscope optical axis (axial motion). Here we have defined a time scale $\tau_{\Delta q}\doteq1/D\Delta q^2$.

It is instructive to study two limit cases for the behavior of $g_z(\mathbf{q},\Delta t)$. For coherent illumination we have

$$g_{z,coh}(\mathbf{q},\Delta t)=\exp[-D_m(q^2/2k_0)^2\Delta t] \tag{54}$$

and, if we take into account Eq. (12), we obtain $g(\mathbf{q},\Delta t)=e^{-D_mQ^2\Delta t}$. This proves that for coherent illumination the motion along one of the three axes contributes to the decay of the correlation function with a term of the form $\exp(-D_mq_i^2\Delta t)$, with $i=x,y,z$. This symmetry is broken with incoherent illumination because

$$g_{z,incoh}(\mathbf{q},\Delta t)=\frac{1}{\sqrt{1+\Delta t/\tau_{\Delta q}}} \tag{55}$$

that represents a slow decay with characteristic time $\tau_{\Delta q}$, which is associated with the wave-vector spread Δq $(\mathbf{q})$. Along the same line of reasoning followed with the single-particle model in Sec. II, we can interpret

$$L(\mathbf{q})=\frac{1}{\Delta q(\mathbf{q})} \tag{56}$$

as the overall q-dependent depth of field for the partially coherent system and $\tau_{\Delta q}$ as the time needed to travel by diffusion a distance on the order of $L(\mathbf{q})$. The existence of a nonzero $L(\mathbf{q})$ is strictly related to the fact that planes progressively far from the object plane contribute less and less to the image. As far as the dynamics is concerned, at the wave vector q we are sensitive not only to the effect of motions of molecules over distances on the order of $1/q$ but also to the effect of diffusion in and out of a region whose size along the optical axis z is on the order of $L(\mathbf{q})$. Equation (56) is the generalization of the results obtained in Eqs. (16) and (20) with the single-particle model. In analogy we require the time scale associated with $L(\mathbf{q})$ being slower than any time scale of interest to ensure that the true dynamics of the system is measured. To facilitate the comparison between the diffusive time $\tau_Q=1/D_mQ^2$ and the spurious time $\tau_{\Delta q}$, we define the dynamic separation ratio

$$r_d(\mathrm{q})\doteq\frac{\tau_Q}{\tau_{\Delta q}}=\frac{\Delta q^2}{Q^2}, \tag{57}$$

which should be kept small for the spurious dynamics to be negligible. It is important to stress that there is a connection between the two parameters $r_s(q)$, which should be kept small for the imaging of phase objects, and $r_d(\mathbf{q})$, which separates the true dynamics from the spurious one. Owing to the fact that $Q^2>\bar{q}_z^2$, we have

$$r_d(q)<r_s(q). \tag{58}$$

From an experimental point of view, this relation guarantees that by optimizing the contrast in the images of phase objects, one gets automatically the best separation between the two dynamic scales. However, $r_d(q)$ can be small despite the value of $r_s(q)$. This is particularly true at low wave vectors because of the fact that $\bar{q}_z^2$ scales as q^4, while Q^2 scales as q^2, which implies that there might be a loss of contrast for phase objects without consequences for dynamic measurements.

E. Finite-size effects

In the previous section we kept the assumption that the sample thickness along the optical axis was infinite. This assumption is well justified if the sample thickness l is larger than $L(q)$. The effect of the finite sample thickness can be incorporated by defining a window function $f(z)$ and performing the substitution $T(\mathbf{q},q_z)\mapsto T(\mathbf{q},q_z)\otimes_{q_z}\hat{f}(q_z)$. A convenient choice is represented by $f(z)=\frac{1}{\sqrt{2\pi}}\exp\{-\frac{1}{2}[(z-z^*)^2/l^2]\}$, where z^* is the distance of the object plane to the sample midplane. The calculation for the general case gives

$$T(\mathbf{q},q_z)=\frac{C(q)\exp\left\{-\frac{1}{2}\left[\frac{\Delta q^2\Sigma^2}{\Delta q^2+\Sigma^2}z^{*2}+\frac{(q_z-\bar{q}_z)^2}{\Delta q^2+\Sigma^2}-\frac{2j\Sigma^2}{\Delta q^2+\Sigma^2}(q_z-\bar{q}_z)z^*\right]\right\}}{\sqrt{2\pi}\sqrt{\Delta q^2+\Sigma^2}}, \tag{59}$$

where we set $\Sigma\doteq 1/l$. The presence of the term $e^{-(1/2)[\Delta q^2\Sigma^2/(\Delta q^2+\Sigma^2)]z^{*2}}$ imposes some requirements on the choice of the object plane because it is responsible of a signal decrease in the images for increasing z^*. This term can be kept small if $z^*\ll\sqrt{l^2+L^2(\mathbf{q})}$ or equivalently if

$$z^*\ll\max\{L(\mathbf{q}),l\}. \tag{60}$$

If the illumination is coherent $[L(\mathbf{q})\to\infty]$ this condition is fulfilled for every value of z^*. On the contrary, whenever $L(\mathbf{q})<l$ the object plane should lie well within the sample. A natural choice is to choose the object plane coincident with the sample midplane ($z^*=0$). In this case Eq. (59) is obtained from Eq. (32) with the substitution

$$\Delta q^2\to\Delta q^2+\Sigma^2. \tag{61}$$

This result is of particular interest because it allows the use of all the previously obtained formulas and does not require additional calculations. In the following we will continue using Δq. Depending on the application, the effect of the sample thickness can be taken into account by using the substitution in Eq. (61).

F. Comparison with the experiments

As anticipated above a quite stringent test of the theory is based on the analysis of the connection between the term $A(q)$ in Eq. (8) and the properties of the microscope. The 73 nm particles investigated here can be considered to a very good extent as phase objects [25] and we have

$$A(\mathbf{q})=2G(\mathbf{q},0)=\frac{2a_P^2}{\sqrt{\pi}}\frac{C^2(\mathbf{q})}{\Delta q}[1-e^{-(\bar{q}_z/\Delta q)^2}] \tag{62}$$

The function $A(q)$ turns out to be related to the coherence properties of the light source (via $\Delta\lambda$ and σ_c) but also to the

cutoff wave vector imposed by the numerical aperture σ_o of the objective. In addition we can observe a dependence on the sample thickness l (via Σ in Δq). For a sample with finite thickness the limit of Eq. (62) for low q is given by $A(q) \sim q^4$. The fact that the signal becomes very small is due to the fact that the sample is a phase object. This decrease could be avoided by using a phase contrast microscope. At large q the behavior of $A(q)$ is set by $C^2/\Delta q$ that causes a decrease associated with the progressive loss of coherence and with the limited numerical aperture of the collection optics.

It should be mentioned here that all these formulas were derived here under the assumption of pointlike scatterers. We anticipate that, if the size of the scatterer cannot be neglected, the right side of Eq. (62) should be multiplied by the q-dependent scattering pattern (form factor) of the particles [25]. For the measurements performed on the 73 nm particles presented in this paper, the form factor can be neglected and Eq. (62) can be used for fitting the experimental data for $A(q)$ without taking into account the effect of the particle form factor. To facilitate the fitting, we impose the known value $\sigma_o = N_o/2 = 0.425$, which reduces the number of fitting parameters. The result of the fitting procedure is shown in Fig. 8 as a dashed line superimposed to the data points. The agreement of the fit with the theory is impressive especially if we take into account that all the model functions in the theory were assumed to be Gaussian functions to allow for exact calculations. The estimates for the fitting parameters are $M = 0.08 \pm 0.01$, $\Delta\lambda/\lambda_0 = 0.15 \pm 0.02$, and $l = 51 \pm 5$ μm. All of these values are very reasonable. A numerical aperture of the condenser about ten times smaller than the numerical aperture of the objective is compatible with the experimental setup that we used even if we did not characterize experimentally the numerical aperture of the condenser. The spectrum of the Osram H64625HLX, tungsten-halogen lamp was measured with a spectrometer and was found to be fitted by a Gaussian function with $\Delta\lambda/\lambda_0 = 0.14$. Finally, as far as the thickness is concerned, we can attempt to find a correspondence between the Gaussian function used for modeling the capillary and a more realistic flat-top profile. This can be done, for example, by imposing that the two curves have the same area. Under this assumption we estimate an equivalent flat-top sample thickness of $l_{eq} = \sqrt{2\pi} l = 130$ μm. Despite the crudeness of this approximation, this value is in fair agreement with the nominal value (100 μm) for the capillary thickness.

As an additional check of our theory, Eq. (62) can be inserted to Eqs. (6) and (8) to model the growth of the variance with Δt. However, an analytical formula cannot be calculated. In Fig. 3 we plot as a continuous line the result of numerical calculations obtained with the parameters extracted from the fitting $A(q)$ and $\tau_d(q)$. The agreement with the experimental data is excellent, given that no adjustable parameters are used.

IV. GENERALIZATION TO LINEAR SPACE-INVARIANT IMAGING SYSTEMS

A. Linear space-invariant three-dimensional imaging

An exhaustive analysis of the process of three-dimensional (3D) image formation is a challenging task whose details depend on the physical process involved (fluorescence, scattering, etc.). The reason why we chose the form expressed by Eq. (23) for the description of microscope images is that Eq. (23) describes an imaging system that is capable of maintaining a *linear space-invariant* relationship between the intensity $I(\mathbf{x},t)$ measured in the image plane and the density $c(\mathbf{x},z,t)$ of our particles. In bright-field microscopy the objects could be scattering centers such as colloidal particles as well as assemblies of molecules. The cases of dark-field microscopy or microscopy of multiple scattering media are not accounted for by our description because they cannot be described by Eq. (23). Other forms of microscopy can be described by Eq. (23) provided that the correct kernel $K(\mathbf{x},z)$ is chosen. For the case of bright-field microscopy, $\tilde{K}(\mathbf{q},q_z)$ describes the so-called 3D OTF [36]. A form of microscopy that falls within this category is represented by fluorescence microscopy.

B. Example: Fluorescence microscopy

In fluorescence experiments $c(\mathbf{x},z,t)$ describes the concentration of the fluorophores that originate the fluorescence signals. In this case, the function $K(\mathbf{x},z)$ coincides with the 3D point spread function for fluorescent imaging. We assume that our sample is fluorescently labeled and each point $(\mathbf{x},z)$ emits a spherical wavelet whose intensity is proportional to the local density $c(\mathbf{x},z)$ multiplied by the intensity of the excitation wave $I_e(\mathbf{x},z)$ in that point. There is no phase relationship between two distinct points and their contributions sum up on an intensity basis. We assume that the fluorescent emission takes place at one single wavelength λ_f or equivalently that this situation is achieved by suitable narrow-band filtering of light. The result will be proved to be independent on the wavelength of the fluorescent emission.

Before turning to the mathematical description of the fluorescence imaging process, it is worth pointing out the main difference between the scattering- and the fluorescence-based dynamic imaging. In analogy to what is done in Fig. 9, we plot in Fig. 14 a simulated pictorial image of the pattern caused by a fluorescent object placed in various positions.

It appears that, in the same way as it was observed for the scattering case, a motion of the particle in the (x,y) plane corresponds to a translation of its pattern in the image plane. On the other hand, a motion along the optical axis z (defocusing) is not related anymore to a shift of interference fringes but is rather connected to a different degree of sharpness of the image. As we will see below the only difference with respect to the scattering-based imaging is related to the dynamics along the z direction.

By dropping the term I_o in Eq. (23) and assuming a constant excitation profile over the sample plane, we obtain

$$\hat{K}(\mathbf{q},z) = \exp\left[-\frac{1}{2}[1+(z\sigma_o^2 k_f)^2]\frac{q^2}{2\sigma_o^2 k_f^2}\right], \tag{63}$$

$$\tilde{K}(\mathbf{q},q_z) = \frac{C(\mathbf{q})}{\sqrt{2\pi}\Delta q(\mathbf{q})}\exp\left[-\frac{1}{2}\left(\frac{q_z}{\Delta q(\mathbf{q})}\right)^2\right], \tag{64}$$

where

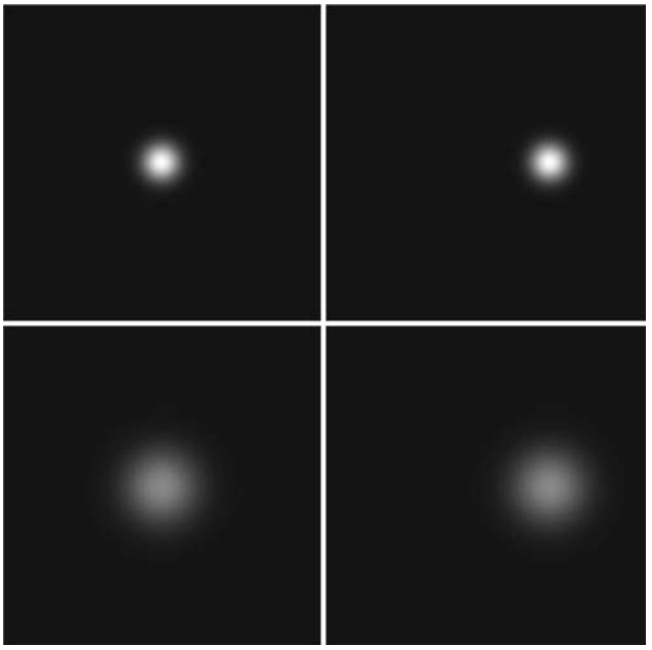

FIG. 14. Simulated pattern generated at some distance from a fluorescent pointlike object (particle), illuminated by a plane, which propagates along the z direction. (Upper left) the particle is in (x_0,y_0,z_0) where z_0 labels the nominal objective plane of the microscope; (upper right) the particle is in $(x_0+\Delta x, y_0+\Delta y, z_0)$. The pattern is unchanged and translated in the (x,y) plane by an amount $(\Delta x,\Delta y)$; (lower left) the particle is in $(x_0,y_0,z_0+\Delta z)$, i.e., further away from the image plane. The pattern did not translate in the (x,y) plane but its shape has changed because of the defocusing distance Δz; (lower right) the particle is in $(x_0+\Delta x, y_0+\Delta y, z_0+\Delta z)$. The pattern translated in the (x,y) plane by an amount $(\Delta x,\Delta y)$ and also modified by virtue of the particle axial displacement Δz.

$$C(\mathbf{q}) = \exp\left[-\frac{1}{2}\left(\frac{q}{q_{ro}}\right)^2\right] \tag{65}$$

with

$$q_{ro} = 2\sigma_o k_f, \tag{66}$$

$$\Delta q^2(\mathbf{q}) = \tfrac{1}{2}\sigma_o^2 q^2. \tag{67}$$

The main result for Brownian diffusion of small particles reads

$$g(\mathbf{q},\Delta t) = \frac{\exp\left(-\dfrac{\Delta t}{\tau_q}\right)}{\sqrt{1+\dfrac{\Delta t}{\tau_{\Delta q}}}}, \tag{68}$$

where

$$\tau_q = \frac{1}{D_m q^2}. \tag{69}$$

The functional form of Eq. (68) shares some similarities with the one appearing in the well-known fluctuation correlation spectroscopy (FCS) technique. The setup for FCS is equivalent to the one for DLS, i.e., is a far-field scattering setup. By contrast with DLS the signal analyzed is the fluorescence intensity that exhibits fluctuations due to the fluctuating number of particles within the scattering volume. For this reason the number of particles is usually kept very small and particle concentrations on the order of nM are typically used. This number fluctuation gives rise to a square-root term identical to the one in Eq. (68). However, in the microscope-based dynamic experiment proposed here, the square-root term is associated only with the depth of focus $L(q)$, while the dynamics in the (x,y) plane coincides with the one that would be measured in a DLS experiment. The former has a typical time scale $\tau_{\Delta q}$ and the latter has τ_q. Under typical experimental conditions, $\tau_{\Delta q} \gg \tau_q$ and the mutual relevance of these two time scales can be expressed by the dynamic separation ratio

$$r_f(\mathbf{q}) = \frac{\sigma_o^2}{2}, \tag{70}$$

which should be kept small for neglecting the number fluctuation term. It must be pointed out that working with large numerical apertures in this case is not beneficial. Finally, we note that Eqs. (65) and (66), valid for the fluorescence case, are strictly connected to the incoherent limit ($M\to\infty$) of Eqs. (36) and (37), valid for the scattering based imaging. In the same way the axial correction in Eq. (68) coincides with Eq. (55).

V. ANALYSIS OF THE DATA

In this Section we give a brief overview on a set of possible algorithms that can be employed for the analysis of dynamic microscopy data. In principle there are at least three ways of analyzing sequences of images.

(1) The image structure function $D(\mathbf{q},\Delta t)$ is calculated as explained above by analyzing pairs of images separated in time by Δt. This was done in Refs. [10,11,13,18,19] where the method was proved to be very efficient in the subtraction of time-independent noise contributions on the images such as, for example, dust particles along the optical path or bad camera pixels. In addition the structure function processing is known to be superior to the correlation function for data subjected to slow temporal drifts [23,22]. This is often the case in microscopy where the average intensity might fluctuate on a slow time scale.

(2) The power spectrum is obtained from each image $I(\mathbf{x},t)$. For every wave vector $\mathbf{q}$ the temporal autocorrelation function (or equivalently the temporal power spectrum or structure function) is calculated. This method may suffer from the presence of the very large static contribution due to the transmitted beam, especially if the latter is modulated in space. However, in some cases it might be used quite profitably, especially when real-time fast processing of the data is useful.

(3) Another alternative that lies in between the two methods consists of using the fact that the signal to be analyzed fluctuates in a stochastic manner around its average intensity, which might have a space-dependent pattern $I_0(\mathbf{x})$. If this average does not change sensibly in time, it can be deter-

mined by averaging many independent frames and subtracted to the individual frames. In this way it is still possible to work on the power spectrum of the difference signal $\delta I(\mathbf{x},t)=I(\mathbf{x},t)-I_0(\mathbf{x})$. This choice is optimal in the presence of a very stable background and it allows us to analyze the data with the structure function, with the correlation function, or with the temporal power spectrum.

It is clear that the algorithms described above are characterized by a lower limit for the experimentally accessible correlation time that is given by the inverse of the camera frame rate. To overcome this limitation a variant has been recently proposed [37,38] that is a q-resolved generalization of the well-known laser contrast speckle analysis (see Ref. [39] for a recent review) and speckle visibility spectroscopy [40]. This procedure allows us to characterize motions at time scales on the order of μs and can also be combined with the differential algorithms outlined above, provided that the time delay between successive images is kept sufficiently large. Additional details can be found in Ref. [38].

VI. CONCLUSIONS

We developed a paraxial theory for the description of the dynamic imaging of weakly scattering 3D objects. Our theory describes the main findings of our benchmark experiment: a bright-field microscopy experiment performed on a colloidal dispersion, analyzed using the DDM method [19]. The theory provides useful criteria for experimental planning, in addition to the quantitative description of dynamic microscopy experiments. The theory encompasses also the previously demonstrated case of near-field scattering dynamic experiments with coherent light [10,11,38]. Interestingly the use of light with a limited degree of coherence sets a q-dependent depth of field [Eqs. (42) and (56)], which in principle limits the accessible wave-vector range. To quantify these limitations we introduced a single-particle model, from which we extract semiquantitative indications about optimized experimental conditions [see Eqs. (18) and (22)]. The model outlines the importance of the numerical aperture of the microscope condenser and of the spread $\Delta\lambda$ of the light source. A more quantitative statement is given in terms of a full theory, which quantitatively accounts for the limitations set by the degree of coherence of the illuminating light. An important result of the theory is that these limitations would appear at wave vectors where the signal is too low to be measured, as expressed by Eq. (58). From a practical point of view a limited coherence turns out to be beneficial in reducing the disturbing fringes that appear when multiple reflections of coherent light from the cell walls interfere on the camera sensor. In fact, the wave-vector range accessed in the present work with DDM turns out to be even wider than the one investigated in previous work with coherent illumination [11]. It has to be pointed out that the DDM data presented here were obtained in a range of scattering angles $[1^\circ,25^\circ]$, which makes DDM a good complementary technique with respect to DLS, as shown in Fig. 7.

With respect to existing dynamic microscopy techniques such as, for example, dynamic light scattering microscopy [41] and defocusing microscopy [42], the distinctive feature of Fourier-based microscopy techniques such as DDM is related to the possibility of characterizing the dynamics of the samples in the wave-vector space. The use of software Fourier transforms of real-space data is in principle equivalent to the direct recording of optical Fourier transforms in the focal plane of a lens [5]. A detailed discussion of the advantages of software processing of near-field images over the traditional far-field schemes can be found in Ref. [17]. Here, we mention that the differential algorithm typical of DDM offers unique performances in terms of background subtraction. Also, it requires no modifications on the microscope. A possible limitation is related to the fact that the fluctuating component of the intensity is superimposed to the most intense transmitted beam and this can impair the characterization of low-scattering samples. On the other hand, the possibility of using an ordinary unmodified microscope for dynamic measurements is appealing in light of the fact that many modern laboratories are already equipped with a microscope. In addition we believe that dynamic microscopy techniques could provide useful insights in all those cases where a space-resolved study of the dynamics is of interest but q-resolved information is also precious. Indeed, as a future extension we envision the possibility of dividing the original images in panels and analyze the dynamics in each panel separately as done, for example, in Ref. [43] for laser velocimetry applications. Such a space-resolved approach would represent a major step forward in the study of soft and biological matter.

ACKNOWLEDGMENTS

R.C. thanks Alberto Vailati for stimulating discussions. R.C. acknowledges financial support from the European Union (Marie Curie Intra-European Action Contract No. EIF-038772) and V.T. from the Swiss National Science Foundation.

[1] *Soft-Matter Characterization: Scattering, Imaging and Manipulation*, edited by R. Pecora and R. Borsali (Springer, Berlin, 2008).

[2] J. C. Crocker and D. G. Grier, J. Colloid Interface Sci. **179**, 298 (1996).

[3] P. Habdas and E. R. Weeks, Curr. Opin. Colloid Interface Sci. **7**, 196 (2002).

[4] B. J. Berne and R. Pecora, *Dynamic Light Scattering: With Applications to Chemistry, Biology, and Physics* (Dover, New York, 2000).

[5] P. D. Kaplan, V. Trappe, and D. A. Weitz, Appl. Opt. **38**, 4151 (1999).

[6] M. Wu, G. Ahlers, and D. S. Cannell, Phys. Rev. Lett. **75**, 1743 (1995).

[7] M. Giglio, M. Carpineti, and A. Vailati, Phys. Rev. Lett. **85**, 1416 (2000).
[8] D. Brogioli, A. Vailati, and M. Giglio, Appl. Phys. Lett. **81**, 4109 (2002).
[9] F. Ferri, D. Magatti, D. Pescini, M. A. C. Potenza, and M. Giglio, Phys. Rev. E **70**, 041405 (2004).
[10] F. Croccolo *et al.*, Appl. Opt. **45**, 2166 (2006).
[11] D. Magatti *et al.*, Appl. Phys. Lett. **92**, 241101 (2008).
[12] I. Rehberg, S. Rasenat, M. de la Torre Juarez, W. Schopf, F. Horner, G. Ahlers, and H. R. Brand, Phys. Rev. Lett. **67**, 596 (1991).
[13] F. Croccolo, D. Brogioli, A. Vailati, M. Giglio, and D. S. Cannell, Phys. Rev. E **76**, 041112 (2007).
[14] C. J. Takacs, G. Nikolaenko, and D. S. Cannell, Phys. Rev. Lett. **100**, 234502 (2008).
[15] R. Cerbino, Phys. Rev. A **75**, 053815 (2007).
[16] A. Gatti, D. Magatti, and F. Ferri, Phys. Rev. A **78**, 063806 (2008).
[17] F. Scheffold and R. Cerbino, Curr. Opin. Colloid Interface Sci. **12**, 50 (2007).
[18] R. Cerbino *et al.*, Nat. Phys. **4**, 238 (2008).
[19] R. Cerbino and V. Trappe, Phys. Rev. Lett. **100**, 188102 (2008).
[20] E. R. Weeks *et al.*, Science **287**, 627 (2000).
[21] C. J. Oliver and E. R. Pike, Opt. Acta **29**, 1345 (1981).
[22] E. O. Schulz-DuBois and I. Rehberg, Appl. Phys. (Berlin) **24**, 323 (1981).
[23] K. Schätzel, Opt. Acta **30**, 155 (1983).
[24] B. Chu, *Laser Light Scattering: Basic Principles and Practice* (Dover, New York, 2007).
[25] H. C. van de Hulst, *Light Scattering by Small Particles* (Dover, New York, 1981).
[26] J. Sheng, E. Malkiel, and J. Katz, Appl. Opt. **45**, 3893 (2006).
[27] J. P. Guigay, Optik (Stuttgart) **49**, 121 (1977).
[28] S. P. Trainoff and D. S. Cannell, Phys. Fluids **14**, 1340 (2002).
[29] P. Cloetens *et al.*, Appl. Phys. Lett. **75**, 2912 (1999).
[30] J. M. Cowley, *Diffraction Physics*, 3rd ed. (revised) (North-Holland, Amsterdam, 1995).
[31] N. Streibl, J. Opt. Soc. Am. A **2**, 121 (1985).
[32] I. Nemoto, J. Opt. Soc. Am. A **5**, 1848 (1988).
[33] H. H. Hopkins, Proc. R. Soc. London, Ser. A **231**, 91 (1957).
[34] M. Born and E. Wolf, *Principles of Optics*, 7th ed. (Cambridge University Press, Cambridge, England, 1999).
[35] P. N. Pusey, *Liquids, Freezing and the Glass Transition* (North-Holland, Amsterdam, 1991).
[36] J. W. Goodman, *Introduction to Fourier Optics*, 3rd ed. (Roberts & Company, Englewood, 2005).
[37] J. Oh, J. M. Ortiz de Zarate, J. V. Sengers, and G. Ahlers, Phys. Rev. E **69**, 021106 (2004).
[38] D. Brogioli *et al.*, Opt. Express **16**, 20272 (2008).
[39] J. D. Briers, Opt. Appl. **37**, 139 (2007).
[40] R. Bandyopadhyay *et al.*, Rev. Sci. Instrum. **76**, 093110 (2005).
[41] R. Dzakpasu and D. Axelrod, Biophys. J. **87**, 1279 (2004).
[42] L. G. Mesquita, U. Agero, and O. N. Mesquita, Appl. Phys. Lett. **88**, 133901 (2006).
[43] M. D. Alaimo *et al.*, J. Appl. Phys. **102**, 073113 (2007).